Title
Density Functional Theory Investigation of Proton Diffusion in Tungsten Oxide And Its Hydrates

Author
Lin, Hao

Publication Date
2014

Peer reviewed|Thesis/dissertation

University of California

Los Angeles

Density Functional Theory Investigation of Proton Diffusion in Tungsten Oxide And Its Hydrates

A thesis submitted in partial satisfaction

of the requirements for the degree

Master of Science in Materials Science and Engineering

by

Hao Lin

2014

Abstract of the Thesis

Density Functional Theory Investigation of Proton Diffusion in Tungsten Oxide And Its Hydrates

by

Hao Lin

Master of Science in Materials Science and Engineering

University of California, Los Angeles, 2014

Professor Vidvuds Ozoliņš, Chair

Fast proton conduction mechanism is of key importance for achieving high performance in fuel cell membranes, batteries, supercapacitors, and electrochromic materials. Enhanced proton diffusion is often observed in hydrated materials where it is thought to occur via the famous Grotthuss mechanism through pathways formed by structural water. Using first-principles calculations, we demonstrate that proton diffusion in tungsten oxide dihydrate ($WO_3 \cdot 2\,H_2O$), a known good proton conductor, takes place within the layers of corner-sharing WO_6 octahedra without direct involvement of structural water. The calculated proton migration barrier in $WO_3 \cdot 2\,H_2O$ is in good agreement with the experimental value inferred from the temperature dependence of conductivity. The preferred proton diffusion path in $WO_3 \cdot 2\,H_2O$ is essentially the same as in γ-WO_3. In contrast to the small intercalation voltages calculated for WO_3 and $WO_3 \cdot 2\,H_2O$, we find that proton absorption in the monohydrate $WO_3 \cdot H_2O$ is energetically highly favorable. However, strong proton-proton repulsion limits the equilibrium H content at zero voltage. We find a fast one-dimensional diffusion channel in $WO_3 \cdot H_2O$ at dilute proton concentrations, but much higher barriers are expected at near-equilibrium concentrations due to strong repulsive interactions with other protons. Our re-

sults illustrate that low proton diffusion barriers and low insertion voltages both contribute to fast proton transport in bulk $WO_3 \cdot 2\,H_2O$ and γ-WO_3.

The thesis of Hao Lin is approved.

Bruce S. Dunn

Yang Yang

Vidvuds Ozoliņš, Committee Chair

University of California, Los Angeles

2014

To my family.

Table of Contents

List of Figures

List of Tables

Acknowledgments

I would foremost like to thank my advisor, Professor Vidvuds Ozoliņš. Vidvuds' passion and creativity were a persistent inspiration throughout my graduate life at UCLA. I was also deeply influenced by his magnetic personality.

I thank Professors Bruce S. Dunn and Yang Yang on my thesis committee for your time in evaluating my thesis. Their insightful and thought-provoking lectures also benefitted me a lot. I would like to thank my collaborators at UCLA: Professor Dunn, Hyungseok Kim and Jesse Ko and at UC Berkeley: Professor Mark Asta, Hong Ding and Keith Ray.

Dr. Fei Zhou, Weston Nielson and Chi-Ping Liu provided me great help since I joined the group. I had great time collaborating with them. I also treasured the discussions with all other members in my group: Yi Xia, Chao Yu, Biljana Rolih and Jiatong Chen.

I cannot thank anyone more than my parents for their endless love and unwavering support throughout my life. It would be impossible for me to complete my journey at UCLA without their encouragements.

CHAPTER 1

Introduction

1.1 Motivation

With the recent development of modern condensed matter theories, improved numerical methods and ever increasing computational power, scientists and engineers have created a new era in which the accuracy of material investigations by theoretical approaches can rival and in some case surpass, that by experimental methods. Fundamental understanding of microscopic mechanisms on the atomic scale can be obtained in computational studies, often more easily than through traditional experimental approaches. A typical example is proton diffusion, which is notoriously difficult to study through experiments but computational tools can shine light into this hard-to-reach realm.

The primary object of this thesis is to provide a fundamental understanding of proton transport in metal oxides and hydrates via density-functional theory (DFT). A better understanding of such reaction mechanism in these materials will aid in the design of higher performance electrochemical energy storage materials.

1.2 Energy storage

Modern society is heavily reliant on energy generated from the burning of fossil fuel, a trend of which has been swiftly growing over the last 50 years. However, the finite availability of fossil fuels, in addition to the associated climate concerns have

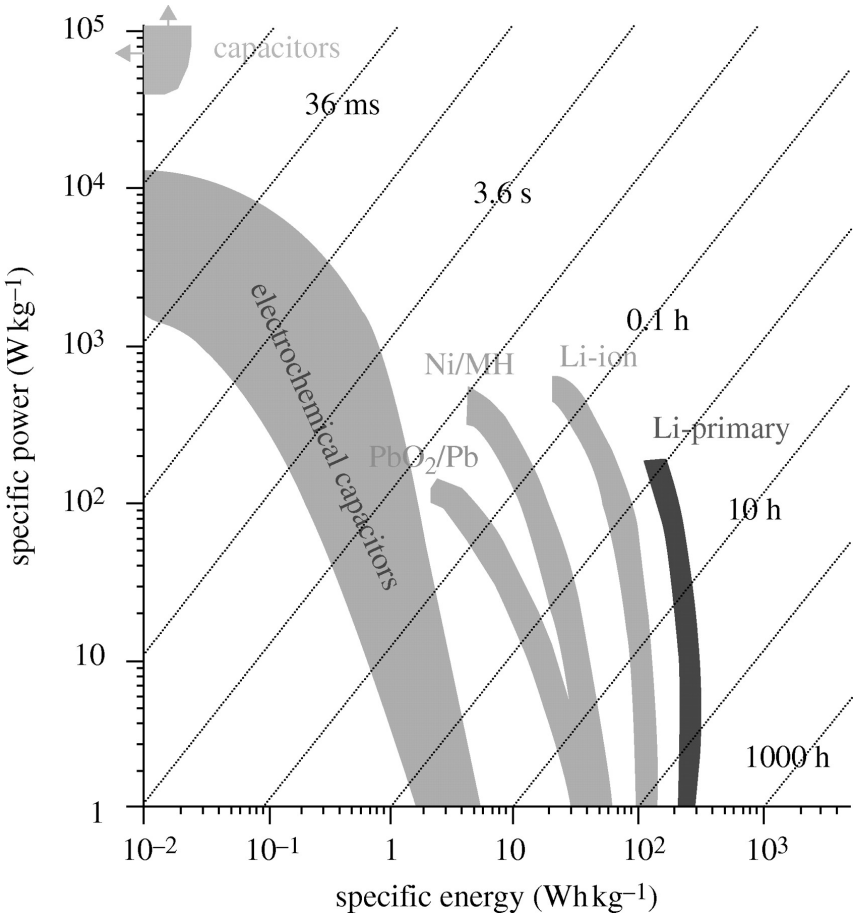

Figure 1.1: A Ragone plot shows energy density and power of various electrochemical energy storage systems from Reference [1]. Reprinted with permission from Nature Publishing Group .

spurred a movement to find alternative, renewable and clean energy generation and storage solutions. Electrochemical energy storage (EES) is one such possible solution. Green electrical energy, which is derived from solar radiation, wind or hydroelectric power, can be stored in EES systems. However, EES technologies for large-scale energy storage have been elusive. For example, hybrid electrical vehicles (HEV), plug-in hybrids and all-electric vehicles still suffer from the lack of reliable energy storage systems with high specific power and high specific energy. Improvements in energy density, reliability and efficiency of EES systems are necessary.

Energy density and power density are two main attributes that characterize the performance of EES systems. Rechargeable batteries and electrochemical capacitors distinguish themselves from other EES systems by their unique combination of energy density and power density. Figure 1.1, known as a Ragone plot, shows the energy density and the power of important EES systems on the market. Due to the high specific power, electrochemical capacitors can be discharged and charged within seconds. However, the energy density of electrochemical capacitors is low. Therefore electrochemical capacitors are suitable for systems which need high power but utilize that energy over a short period of time. One such application is seaport crane. Electrochemical capacitors can be embedded in rubber-tired gantry cranes and capture waste energy that is generated by the up and down movement of shipping containers [2]. A second important application of electrochemical capacitors is emergency back-up power for computer systems. When a power outage occurs, electrochemical capacitors are able to provide back-up power for computers, allowing important data to be properly saved before the shutdown of the whole system. Lithium batteries are positioned in the lower right of the figure, indicating their high energy density and low power density. Thus, we can use batteries to keep devices, such as cell phones, working for days, but they must be charged for hours before we can reuse them.

The difference in energy density and power density between capacitors and rechargeable batteries comes from fundamentally distinct charge storage mechanisms. There are two charge storage mechanisms for electrical energy in electrochemical energy storage systems. First, charge can be stored electrostatically in materials. This charge storage process, known as non-Faradaic process, usually happens on the surface of materials and often shows excellent reversibility. Charge storage in capacitors is achieved primarily through the non-Faradaic process. The second form of electrical energy storage is achieved via Faradaic oxidation and

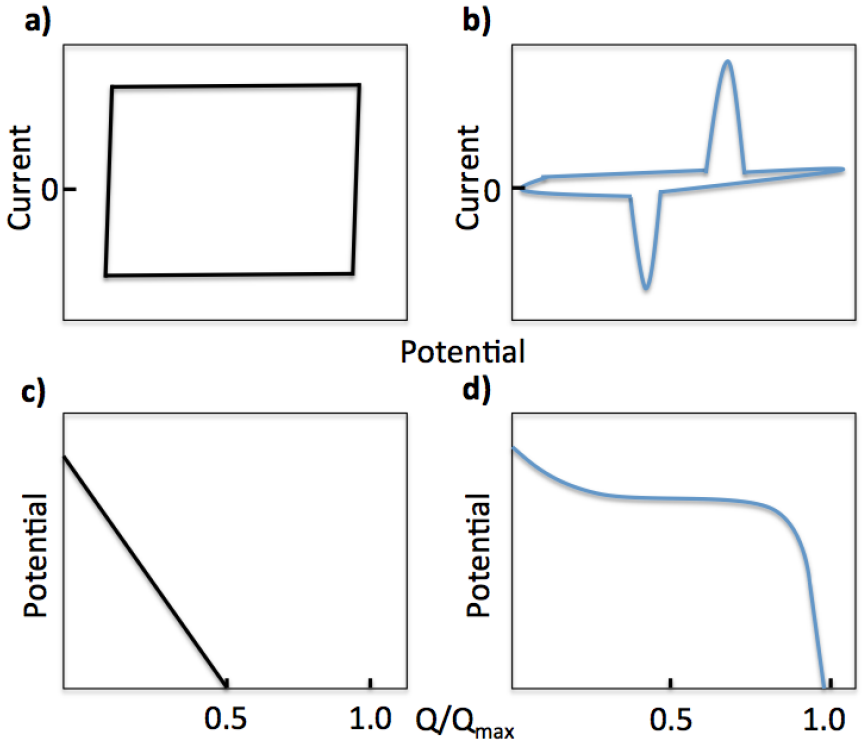

Figure 1.2: Cyclic voltammograms of (a) a capacitor and (b) a battery. Galvanostatic discharge behavior for (c) a capacitor and (d) a battery.

reduction processes, as shown in the following chemical reaction:

$$Ox + ne^- \rightleftharpoons Red, \tag{1.1}$$

where Ox and Red are the oxidized and reduced forms of an electrode material and n is the number of electrons that can be transferred. Charges can flow and perform electric work when there are potential differences between two electrodes. This mechanism is typically observed in batteries.

Cyclic voltammogram and galvanostatic discharge behavior of capacitors and batteries can reflect the differences in their inherent charge storage mechanisms. (See Figure 1.2) The cyclic voltammogram of a capacitor is typically rectangular in shape and lacks any distinct redox peaks (Figure 1.2a). In addition, the galvanostatic discharge curve shows that the voltage changes linearly at a constant

current (Figure 1.2c). The energy (G) of the discharging of a capacitor is the product of the capacitance (C) and the square of the voltage (V), shown via the following formula:

$$G = \frac{1}{2}CV^2. \tag{1.2}$$

In capacitors, the voltage is usually not related to the chemical potentials of electrode materials. The maximum voltage applied to a capacitor is limited by the electrochemical window of the electrolyte. In practice, when the voltage of a capacitor is larger than the breakdown voltage, substantial leakage current occurs in the electrolyte and leads to the failure of the capacitor. The capacitance is determined by the geometry of the electrode materials and the dielectric property of the electrolyte:

$$C = A\epsilon/d, \tag{1.3}$$

where A is the surface area of the electrode, d is the spacing between two electrodes and ϵ is the permittivity. It can be seen that the amount of energy that can be stored in capacitors is governed by the capacitance and the voltage.

In contrast, the cyclic voltammogram of a battery shows distinguishable redox peaks, indicating there is a phase change during the discharge (see Figure 1.2b). Phase changes in battery materials may lead to thermodynamic irreversibility. The separation of oxidized and reduced peaks is due to the polarization of the device. As shown in Figure 1.2d, the voltage plateau in galvanostatic discharge curve indicates the presence of two phases during the discharge. The energy stored in batteries is given by:

$$G = -qV, \tag{1.4}$$

where q is the electric charge. The theoretical charge q of a material can be calculated by Faraday's laws of electrolysis:

$$q = \frac{nF}{M}, \tag{1.5}$$

where n is the number of electrons transferred in one reaction, F is the Faraday constant, which equals 96,485 C/mol, and M is the molar mass of the electrode material.

To summarize, electrochemical capacitors commonly have a high degree of reversibility (10^4–10^6 cycles) due to the non-Faradaic process during the charge-discharge cycle. Capacitors show an almost constant current profile in response to a linear change of potential. Additionally, a linear decline of potential is observed when capacitors are discharged at constant current. As for batteries, the efficiency decreases to 90 percent after 10^3–10^4 cycles because phase transition in the materials leads to thermodynamic and kinetic irreversibility. The current profile is not constant in response to linear modulation of potential, while the potential remains a constant with unchanged discharge current.

1.3 Comparison of two types of capacitors

The capacitors discussed in Section 1.2 are called electric double-layer capacitors, which store charge mainly through non-faradaic mechanism. There is, however, another type of capacitor, known as a pseudocapacitor, that stores charge via the Faradaic process. The electrochemical behavior of pseudocapacitors is similar to that of electric double-layer capacitors, even though the charge storage is accomplished by chemical reactions in the electrode materials. The main differences in the charge storage mechanisms between electric double-layer capacitors and pseudocapacitors are shown in Figure 1.3.

In electric double-layer capacitors, charges are stored by electrostatic separation of positive and negative charges in two separated electrodes. As drawn in the left of Figure 1.3, the positive charges in one of the electrodes attract the opposite charges in the electrolyte with the same amount, forming electric double layer at the electrode/electrolyte interface [3]. Due to their high surface area and high

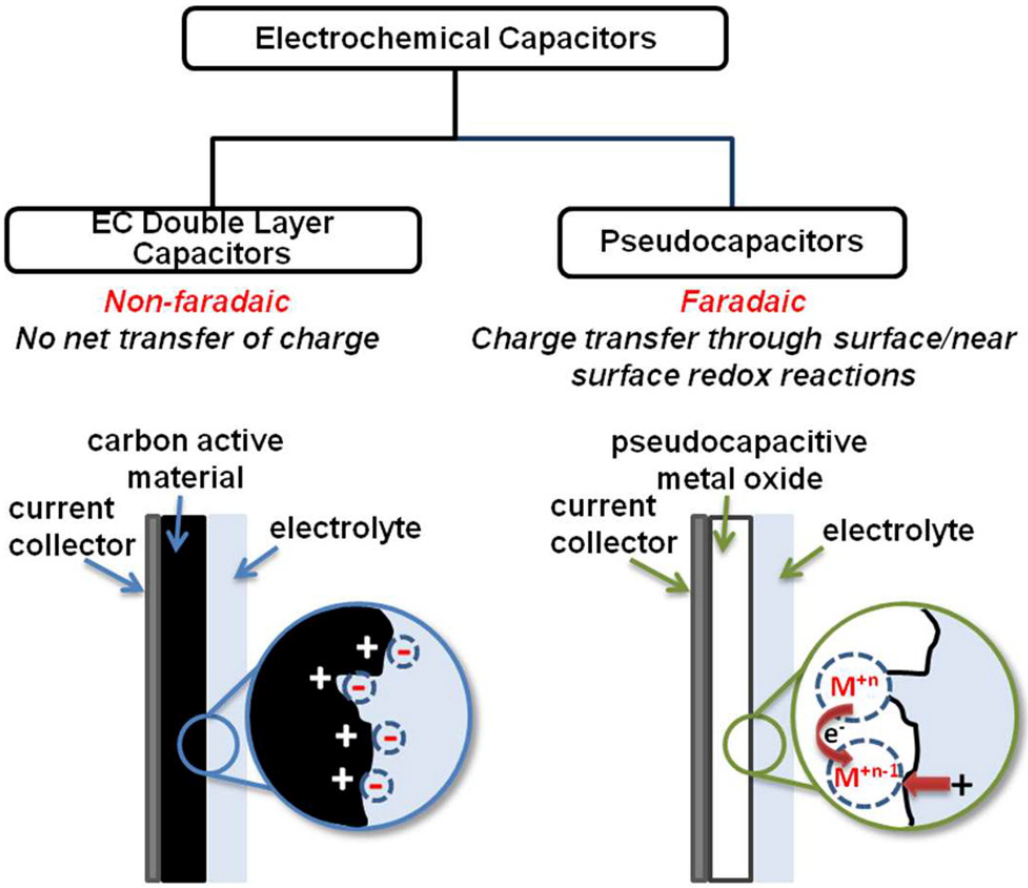

Figure 1.3: Two types of electrochemical capacitors. Adapted with permission from Reference [3]. Copyright (2013) American Chemical Society.

electronic conductivity, activated carbon materials are used as electrodes.

In pseudocapacitors, the chemisorption of ions (A) in electrode materials leads to the partial charge transfer in an electrode (M) [4]:

$$M + A^- \rightleftharpoons M/A^{(1-\delta)-} + \delta e(in\, M). \tag{1.6}$$

Such a Faradaic redox reaction happens at the surface of the electrode material, but phase transitions do not occur during the charge and discharge process, which is different from the redox reactions in battery materials. Transition metal oxides, such as Ruthenium oxide (RuO_2) and Iridium oxide (IrO_2), are usually used as

pseudocapacitive electrode materials. Ruthenium oxide was first investigated as a pseudocapacitive material by Trasatti *et al* in 1971 [5]. They found that the cyclic voltammogram of ruthenium oxide has a rectangular shape, which is similar to the behavior of a capacitor. It was later demonstrated by Zheng *et al* that hydrous ruthenia has higher specific capacity and charging rate than the anhydrous ruthenium oxide [6]. The better performance in hydrous ruthenia was recently explained by the fact that fast protonic transport in hydrous ruthenia is due to the existence of structural water at grain boundaries and the activation barrier for proton diffusion in bulk ruthenium oxide is high [7, 8]. Since the specific capacitance of the pseudocapacitors (>600 F/g) is much higher than that in the electric double-layer capacitors (∼150 F/g), understanding the electrochemical principles of the pseudocapacitors is necessary in order to design next-generation electrochemical capacitors with higher energy density.

1.4 Proton diffusion mechanisms

Proton conductivity is a key property of aqueous electrolytes and electrodes for electrochemical capacitors. There are two main proton-conducting mechanisms in aqueous and hydrated materials, as shown in Figure 1.4. In the materials with hydrogen-bonded networks, protons hop from one site to another by breaking and forming hydrogen bonds. This mechanism was first proposed by Grotthuss in 1806 [9]. The hopping of protons is accompanied by the reorientations of O-H groups, H_2O and H_3O^+ in the hydrogen-bonded networks. A continuous proton migration path requires a short distance between the oxygen cations within the hydrogen-bonded networks in addition to the rotation of O-H groups. Therefore, proton hopping rates and reorganization rates of O-H groups are the dominant factors in determining proton conductivity [10]. The second mechanism, called vehicle mechanism (proton-carrying mechanism), transports protons via a "vehicle" such

as H_3O^+, $H_5O_2^+$ and NH_4^+. At the same time, the empty "vehicles" without protons move in the opposite direction [11]. The vehicle diffusion rate largely determines the overall proton conductivity. This mechanism is often observed in water-rich materials or acidic aqueous solutions.

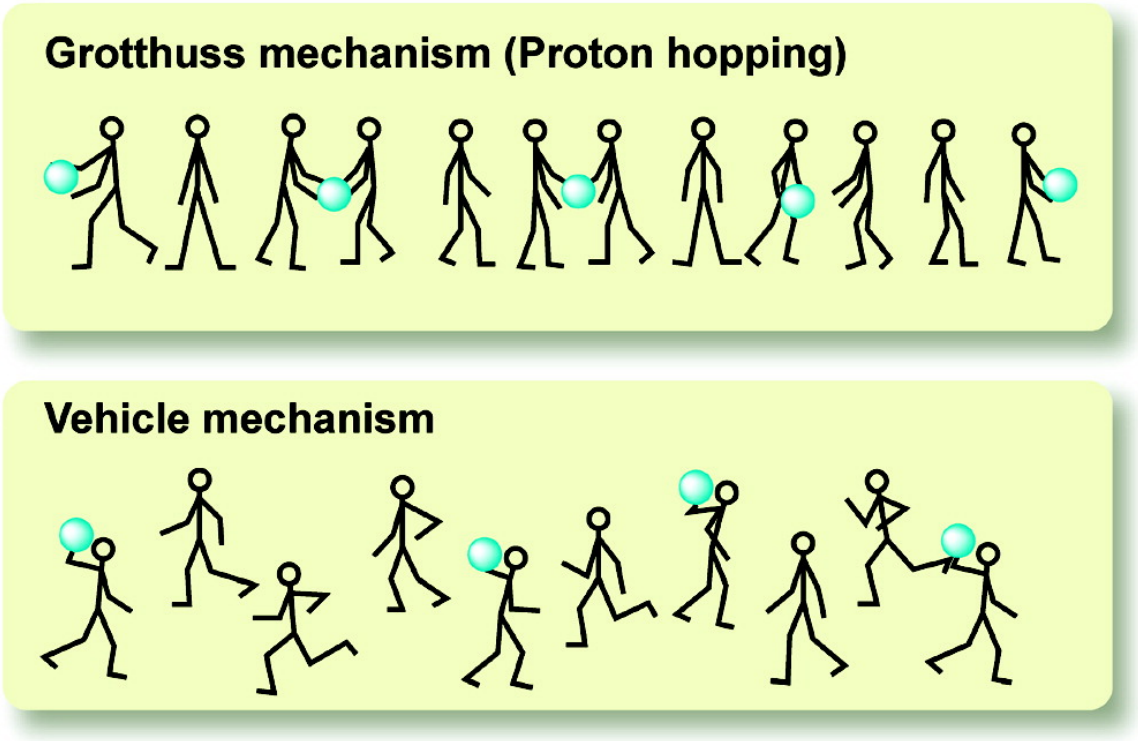

Figure 1.4: Two types of proton diffusion mechanisms. Reprinted with permission from [10]. Copyright (2008) American Chemical Society.

In addition, proton diffusion proceeds via the third mechanism in metal oxides, such as ReO_3, $BaCeO_3$ and $CaTiO_3$ [11, 12, 13]. Typically, such oxides have 2D or 3D networks of corner-sharing MO_6 octahedra and protons prefer to form bonds with oxygen ions. The proton migration is achieved either by the hopping of protons among the neighboring oxygen sites or by the combinations of such hopping and the rotation of protons about the M-O-M axes.

1.5 General Methods

1.5.1 The Born-Oppenheimer approximation

The nature of matter is fundamentally determined by electrons and nuclei. *Ab initio* calculations can predict material properties from the quantum mechanical level and shine light onto the fields that are difficult to investigate through experimental methods. The starting point for solving a quantum mechanical problem is the Shrödinger equation:

$$\hat{H}\Psi = E\Psi, \tag{1.7}$$

where $\hat{H}$ is the Hamiltonian operator, Ψ is the wave function and E is the energy eigenstate. For the system of electrons and nuclei, $\hat{H}$ can be expressed in the following form [14]:

$$\begin{aligned}\hat{H} = -\frac{\hbar^2}{2m_e}\sum_i \nabla_i^2 - \frac{\hbar^2}{2M_I}\sum_I \nabla_I^2 + \sum_{i<j}\frac{e^2}{4\pi\epsilon_0|\boldsymbol{r}_i - \boldsymbol{r}_j|} \\ + \sum_{i,I}\frac{Z_I e^2}{4\pi\epsilon_0|\boldsymbol{r}_i - \boldsymbol{R}_I|} + \sum_{I<J}\frac{Z_I Z_J e^2}{4\pi\epsilon_0|\boldsymbol{R}_I - \boldsymbol{R}_J|},\end{aligned} \tag{1.8}$$

where the first two terms in the right-hand side are the kinetic energy terms of electrons and nuclei, the last three terms are the Coulomb interactions of electron-electron, electron-nuclear and internuclear. Since the nuclear are much heavier than the electrons, the kinetic energy of nuclei can be neglected when calculating electronic wave functions and the motion of nuclei and electrons can be decoupled. Such an approximation is called the Born-Oppenheimer approximation. In this approximation, the ionic contribution to the energy is treated as an external potential on the electrons. Thus, the Hamiltonian can be approximated as

$$\hat{H} = \hat{T} + \hat{V}_{\text{int}} + \hat{V}_{\text{ext}} + E_{\text{nuclei}}, \tag{1.9}$$

where $\hat{T}$ is the kinetic energy operator for electrons, $\hat{V}_{\text{int}}$ is the electron-electron interaction, $\hat{V}_{\text{ext}}$ is the potential acting on the electrons from the nuclei, and E_{nuclei} is the sum of the classic nuclear interaction and any other non-electron interactions. If atomic units have been adopted ($m_e = e = \hbar = \frac{1}{4\pi\epsilon_0} = 1$), then the first three terms can be expressed in a succinct way:

$$\hat{T} = -\frac{1}{2}\sum_i \nabla^2, \tag{1.10}$$

$$\hat{V}_{\text{int}} = \sum_{i<j} \frac{1}{|\boldsymbol{r}_i - \boldsymbol{r}_j|}, \tag{1.11}$$

$$\hat{V}_{\text{ext}} = \sum_{i,I} V_I(|\boldsymbol{r}_i - \boldsymbol{R}_I|). \tag{1.12}$$

1.5.2 The Hohenberg-Kohn theorems

Although the decoupling of the motion of electrons and nuclei by the Born-Oppenheimer approximation can simplify the many-body Shrödinger equation, the wave function is still very complicated due to its dependence on $4N$ variables, where N is the number of the electrons in the system with each electron containing three spatial variables and one spin variable. An alternative approach to tackle this problem is to treat the Hamiltonian as a functional of the electron density $\rho(\boldsymbol{r})$, which at a point $\boldsymbol{r}$ is defined by the following formula:

$$\rho(\boldsymbol{r}) = N\sum_{\sigma}\int ... \int |\Psi(\boldsymbol{r}, \sigma_1, \boldsymbol{r}_2, \sigma_2..., \boldsymbol{r}_N, \sigma_N)|^2 d\boldsymbol{r}_2 d\boldsymbol{r}_3 ... d\boldsymbol{r}_N. \tag{1.13}$$

$\Psi(\boldsymbol{r}, \sigma_1, \boldsymbol{r}_2, \sigma_2..., \boldsymbol{r}_N, \sigma_N)$ is the wave function of the system with N electrons. $\boldsymbol{r}_i$ is the position of the i^{th} electron and σ_i represents its spin state. The electron density satisfies the rule that

$$\int \rho(\boldsymbol{r}) d\boldsymbol{r} = N. \tag{1.14}$$

The relationship between the electron density and the Hamiltonian was described by the Hohenberg-Kohn theorems, which serve as the foundation of the density functional theory [15]. The first Hohenberg-Kohn theorem states that the ground state electron density, $\rho(\boldsymbol{r})$, uniquely determines the external potential, except for a constant. In addition, since the first two terms on the right-hand side in equation 1.9 are obtained by the electron density through equation 1.14, the electron density uniquely determines the Hamiltonian.

The second Hohenberg-Kohn theorem says that for any specified external potential, the global minimum value of the energy functional $E[\rho(\boldsymbol{r})]$ is obtained if and only if the density $\rho(\boldsymbol{r})$ is the ground state density $\rho_0(\boldsymbol{r})$. The combination of these two theorems indicates that the exact ground-state energy of the system can be expressed by the Hamiltonian acting on electron densities:

$$E_0 = \min_{\rho} \{E[\rho]\}, \tag{1.15}$$

$$= \min_{\rho} \left\{ T[\rho] + E_{\text{int}}[\rho] + \int d\boldsymbol{r} V_{\text{ext}}(\boldsymbol{r})\rho(\boldsymbol{r}) + E_{\text{nuclei}} \right\}, \tag{1.16}$$

$$= \min_{\rho} \left\{ F_{\text{HK}}[\rho] + \int d\boldsymbol{r} V_{\text{ext}}(\boldsymbol{r})\rho(\boldsymbol{r}) \right\}, \tag{1.17}$$

where $F_{\text{HK}}[\rho]$, including the kinetic and potential energies of the interacting electron system, is the sum of $T[\rho]$ and $E_{\text{int}}[\rho]$. However, the exact expression $F_{\text{HK}}[\rho]$ is not known. This functional is approximated by different approaches, such as Thomas-Fermi model, orbital-free DFT and Kohn-Sham DFT. The most popular method is the Kohn-Sham formalism which is introduced in the next subsection.

1.5.3 The Kohn-Sham approach

The essence of the Kohn-Sham approach is to approximate the electron wave function as non-interacting electron orbitals $\phi_i(\boldsymbol{r})$ (Kohn-Sham orbitals), with all the complexity of electron interaction grouped into the exchange-correlation

term in the effective potential, $V_{\text{eff}}(\boldsymbol{r})$ [16]. Under this potential, the Kohn-Sham Shrödinger-like equations is

$$[-\frac{1}{2}\nabla^2 + V_{\text{eff}}(\boldsymbol{r})] = \epsilon_i \phi_i(\boldsymbol{r}), \tag{1.18}$$

where the ϵ_i are the energy eigenvalues. The electron density is given by the sum of Kohn-Sham orbitals:

$$\rho(\boldsymbol{r}) = \sum_i |\phi_i(\boldsymbol{r})|^2 \tag{1.19}$$

The $V_{eff}(\boldsymbol{r})$ can be expressed by

$$V_{\text{eff}}(\boldsymbol{r}) = V_{\text{ext}}(\boldsymbol{r}) + V_{\text{H}}(\boldsymbol{r}) + V_{\text{xc}}(\boldsymbol{r}), \tag{1.20}$$

where the Hartree potential,

$$V_{\text{H}}(\boldsymbol{r}) = \int d\boldsymbol{r}' \frac{\rho(\boldsymbol{r}')}{|\boldsymbol{r} - \boldsymbol{r}'|}, \tag{1.21}$$

and the exchange-correlation potential,

$$V_{\text{xc}}(\boldsymbol{r}) = \frac{\delta E_{\text{XC}}[\rho]}{\delta \rho(\boldsymbol{r})}, \tag{1.22}$$

are originated from the electron-electron interaction in equation 1.9.

1.5.4 Exchange-Correlation functionals

The exchange-correlation energy includes the quantum mechanical effects of electron interacting and any other things which are lost in treating the electrons as non-interacting. Thus, the framework of Kohn-Sham DFT provide the possibility to solve the Shrödinger equations exactly. However, the exact form of the exchange-correlation energy is unknown. There are two popular approximations to the exchange-correlation energy, namely the local density approximation

(LDA) [17] and the generalized gradient approximation (GGA) [18], which are widely used in solid state physics.

The local density approximation treats the non-interacting electrons as a uniform electron gas and the exchange-correlation energy can be written as

$$E_{\mathrm{XC}}^{\mathrm{LDA}}[\rho] = \int d\boldsymbol{r}\, \rho(\boldsymbol{r}) \epsilon_{\mathrm{xc}}^{\mathrm{LDA}}[\rho], \tag{1.23}$$

where $\epsilon_{\mathrm{xc}}^{\mathrm{LDA}}[\rho]$ is the exchange-correlation energy per electron and contains the exchange part and the correlation part,

$$\epsilon_{\mathrm{XC}}^{\mathrm{LDA}}[\rho] = \epsilon_{\mathrm{X}}^{\mathrm{LDA}}[\rho] + \epsilon_{\mathrm{C}}^{\mathrm{LDA}}[\rho]. \tag{1.24}$$

Based on Dirac's derivation, the exchange part is given by

$$\epsilon_{\mathrm{X}}^{\mathrm{LDA}}[\rho] = -\frac{3}{4}[\frac{3\rho(\boldsymbol{r})}{\pi}]^{1/3}. \tag{1.25}$$

An exact expression for the correlation part is unknown but it can be obtained from accurate quantum Monte Carlo simulations. The success of LDA has encouraged the development of the generalized gradient approximation. In the GGA, the exchange-correlation energy is a function of both the electron densities and the electron density gradients and it is given by

$$\epsilon_{\mathrm{XC}}^{\mathrm{GGA}} = f(\rho_{\uparrow}, \rho_{\downarrow}, \nabla\rho_{\uparrow}, \nabla\rho_{\downarrow}). \tag{1.26}$$

GGAs have been widely adopted by the physics and chemistry community and the most popular GGA functionals are Perdew-Burke-Enzerhof and Perdew-Wang, etc [18, 19].

CHAPTER 2

Proton diffusion in tungsten oxide and its hydrates

2.1 Introduction

Fundamental understanding of the mechanisms of proton conduction is crucial for the development of fuel cell membranes, batteries, supercapacitors and electrochromics [7, 20, 21]. It is commonly believed that proton diffusion in hydrous materials occurs via a Grotthuss type mechanism facilitated by water molecules [9]. For instance, fast protonic transport in hydrous ruthenia ($RuO_2 \cdot xH_2O$) has been attributed to the existence of structural water at grain boundaries [7]. The appearance of a strongly rate-dependent contribution to the charging capacity of ruthenia at very slow rates suggests that proton diffusion in bulk RuO_2 is kinetically hindered [22], a conclusion which is supported by a high migration barrier found in first-principles calculations [8]. Recently, tungsten oxide dihydrate ($WO_3 \cdot 2\,H_2O$) was observed to have a relatively high proton conductivity (7×10^{-3} S/cm at 423 K) and low proton activation energies for bulk (0.36 eV) and surface (0.15 eV) diffusion [23], demonstrating its potential for use as a proton conductor at low and medium temperatures (273–423 K). The presence of layered water in the crystal structure of $WO_3 \cdot 2\,H_2O$ again seemingly suggests that the Grotthuss mechanism contributes to proton diffusion through this compound, but our knowledge of the actual proton diffusion kinetics in $WO_3 \cdot 2\,H_2O$ is limited. In particular, it remains an open question whether proton transport in $WO_3 \cdot 2\,H_2O$

is mediated by the structural water layer in this compound. A related question is whether the much higher bulk proton conductivity of $WO_3 \cdot 2\,H_2O$ in comparison with the monohydrate, $WO_3 \cdot H_2O$, can be explained by the absence of hydrogen-bonded layers of structural water in the latter.

This chapter reports a comparative first-principles study of proton intercalation and transport in a series of structurally related solids (γ-WO_3, $WO_3 \cdot H_2O$, and $WO_3 \cdot 2\,H_2O$) that incorporate corner-linked networks of WO_6 octahedra. Using density-functional theory (DFT) calculations, we investigate the crystal structures, bonding, electronic properties, proton intercalation energetics, and energy barriers for proton diffusion. In $WO_3 \cdot 2\,H_2O$, we find that intercalated hydrogen donates charge to the empty orbitals in the tungsten oxide layer. Surprisingly, our results show that proton diffusion in $WO_3 \cdot 2\,H_2O$ occurs through the layers of corner-sharing WO_6 octahedra and does not involve the hydrogen-bonded H_2O network in the structural water layer. This is explained by the fact that the preferred adsorption site for the intercalated proton is at one of the bridging oxygen ions where it forms a bond with a nonbonding O $2p$ orbital. Diffusion is facilitated by a low energy cost for a concerted rotation of the interlinked WO_6 octahedra that is involved in "swinging" the adsorbed proton around the bridging oxygen ion. Our calculations show that this configuration is approximately 0.3 eV more favorable than the formation of a hydronium ion (H_3O^+) in the water layer. Since the anhydrous γ-phase WO_3 also contains a corner-linked network of WO_6 octahedra, we find that proton diffusion in this material follows the same mechanism and has a similar activation energy. A more complex behavior is predicted for the monohydrate $WO_3 \cdot H_2O$. At dilute concentrations, protons adsorb at the terminating oxygen site where they can diffuse along one-dimensional zigzag pathways running in the [100] direction between the octahedral layers. The calculated barrier of proton migration along the one-dimensional pathways is low (0.07 eV). In a marked difference from γ-WO_3 and $WO_3 \cdot 2\,H_2O$, hydrogen absorp-

tion in $WO_3 \cdot H_2O$ is energetically highly favorable (by more than 1 eV/H) and the dilute limit is not experimentally relevant. We calculate that at non-dilute concentrations the majority of protons adsorb within the octahedral layers and strong proton-proton repulsion limits the equilibrium zero-voltage hydrogen concentration in $H_yWO_3 \cdot H_2O$ to y values in the 10–20% range. To explain why only surface diffusion contribution is observed for $WO_3 \cdot H_2O$ [23], we hypothesize that the one-dimensional diffusion channels are blocked due to repulsive interactions with the protons in the octahedral layers. We also suggest that the bulk diffusion mechanism predicted for WO_3 and $WO_3 \cdot 2\,H_2O$ is not operational in $WO_3 \cdot H_2O$ at non-dilute concentrations, because adsorbed protons cause a stiffening of the octahedral layer with respect to the rotations of the WO_6 octahedra, inhibiting a key step in the proton diffusion mechanism.

2.2 Methods

The Perdew-Burke-Ernzerhof (PBE) [18] exchange correlation functional and the projector augmented wave (PAW) method [24] as implemented in the Vienna *Ab Initio* Simulation Package (VASP)[25] were used in all our calculations. We used bulk supercells of γ-WO_3 ($WO_3 \cdot H_2O/WO_3 \cdot 2\,H_2O$) containing 32 (16/16) formula units. In all cases, plane wave basis sets with an energy cutoff of 875 eV were used to expand the electronic wave functions, and 2×2×2 Monkhorst-Pack [26] **k** point meshes were used to sample the Brillouin zone. Convergence tests showed that with these settings the total energies were converged to within 2 meV per formula unit, compared to calculations with a 10×10×10 Monkhorst-Pack **k** point mesh. Atomic coordinates were fully relaxed until all forces were below 0.02 eV/Å and cell parameters were relaxed until components of the stress tensor were below 0.4 kbar. Our tests for tungsten oxide dihydrate showed that spin-orbit coupling (SOC) effects increase the calculated proton intercalation voltage by only

0.03 eV, and hence SOC is neglected in the results reported here. Proton diffusion pathways between two locally stable proton sites are calculated using the nudged elastic band (NEB) method[27] with at least five intermediate images. The transition state obtained by NEB was further refined using the climbing nudged elastic band (cNEB) method [28]. Activation barriers presented here include quantum tunneling corrections calculated at 298 K using the formalism of Fermann and Auerbach [29].

In electrochemical experiments, proton intercalation is accompanied by an electron insertion. This process is modeled computationally as insertion of neutral hydrogen atoms. Using the reversible hydrogen electrode as a reference, the voltage of proton insertion in the dilute limit is calculated as [8]

$$V = \frac{\Delta G}{e}, \tag{2.1}$$

where ΔG is the free energy of proton intercalation in bulk $WO_3 \cdot xH_2O$ ($x = 0, 1, 2$). ΔG can be calculated from the following expression:

$$\begin{aligned} \Delta G =& G[H_{m+1}(WO_3 \cdot xH_2O)_n] - G[H_m(WO_3 \cdot xH_2O)_n] \\ & - \frac{1}{2}G^\circ[H_2] \end{aligned} \tag{2.2}$$

where $G[H_m(WO_3 \cdot xH_2O)_n]$ is the total free energy of bulk supercell of $WO_3 \cdot xH_2O$ with m additional hydrogen atoms, $G[H_{m+1}(WO_3 \cdot xH_2O)_n]$ is the total free energy of bulk $WO_3 \cdot xH_2O$ with $m+1$ additional hydrogen atoms, and $G^\circ[H_2]$ is the standard state free energy of hydrogen gas at atmospheric pressure and $T = 298$ K [8].

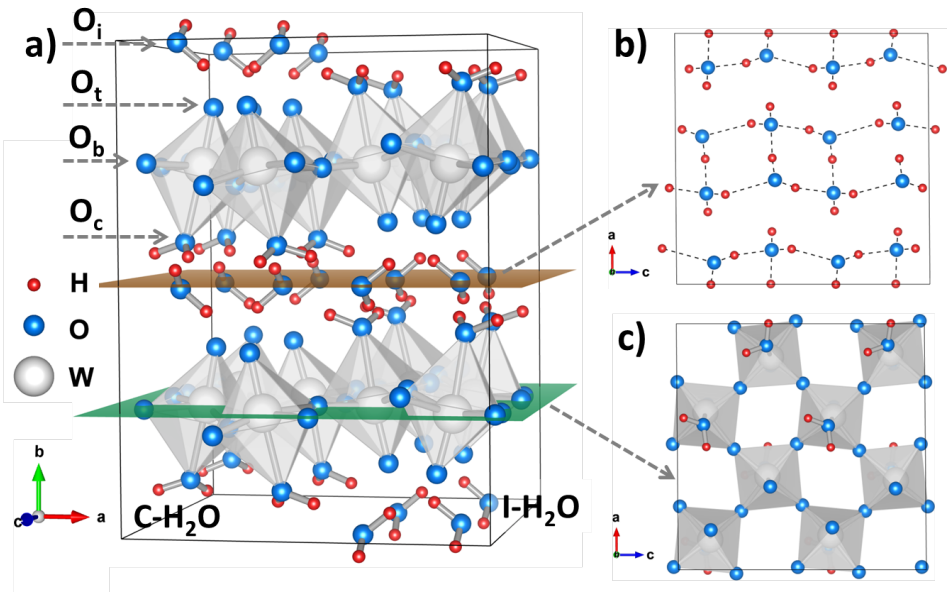

Figure 2.1: a) Crystal structure of tungsten oxide dihydrate, where O_c, O_b, O_t and O_i represent coordinated water oxygen, bridging oxygen, terminating oxygen and oxygen in interlayer water respectively, and C-H_2O, I-H_2O denote coordinated water and interlayer water, b) hydrogen-bonded network, c) a tungsten-oxygen octahedral layer. Protons are shown in red, oxygen ions in blue, tungsten ions in white and WO_6 octahedra in grey.

Table 2.1: A comparison of experimental and calculated crystal parameters (in the unit of Å) of tungsten oxide dihydrate.

Methods	a(Å)	b(Å)	c(Å)	Δa/a	Δb/b	Δc/c
Expt.[23]	10.48	13.97	10.62			
GGA	10.57	14.12	10.67	0.86%	1.07%	0.47%

2.3 Results

2.3.1 Structural properties

The crystal structure of tungsten oxide dihydrate (shown in Figure 2.1a) belongs to the monoclinic $P2_1/n$ space group. This structural framework consists of a connected network of corner-sharing WO_6 octahedra (shown in grey in Figure 2.1c) and two types of water molecules. The first type, called "coordinated water", shares its oxygen with the tungsten ion, while the other, referred to as "interlayer

water", is located within the (010) plane between the layers of WO_6 octahedra (see Figure 2.1a and 2.1b). As marked in Figure 2.1a, there are four types of oxygen sites in $WO_3 \cdot 2\,H_2O$: coordinated water oxygen (O_c), bridging oxygen (O_b), terminating oxygen (O_t), and interlayer water oxygen (O_i). Within the distorted octahedra, the relaxed W-O_b bond lengths range from 1.86 to 2.03 Å, and the distance between the W and O_t ions is 1.75 Å, much shorter than the length of the W-O_c bond (2.31 Å). The variation in W-O bond lengths is due to different types of bonding: (1) an O_t ion is only bonded to a W ion, (2) each O_b ion is bonded to two W ions within octahedral planes, and (3) weak W-O_c bonding because of strong O_cH bonding in the sp^3 hybridization. A more detailed analysis of the electronic structure and bonding in $WO_3 \cdot 2\,H_2O$ is given in Section 2.3.2.

Rietveld refinement results for $WO_3 \cdot 2\,H_2O$ do not contain the coordinates of hydrogen atoms because the XRD patterns of $WO_3 \cdot 2\,H_2O$ were determined by Cu-Kα radiation (1.54056 Å), which has a longer wavelength than typical O-H distances [23]. Since $WO_3 \cdot 2\,H_2O$ and $MoO_3 \cdot 2\,H_2O$ share the same space group and exhibit identical arrangements of the metal and oxygen ions, we obtained the structure of $WO_3 \cdot 2\,H_2O$ by taking the hydrogen positions from the crystal structure of $MoO_3 \cdot 2\,H_2O$ as input and relaxing all degrees of freedom. As listed in Table 2.1, the calculated a, b and c lattice parameters are 10.57, 14.12, and 10.67 Å, respectively, slightly larger than the experimental values (a = 10.48, b = 13.97, and c = 10.62 Å), while the relaxed value of the monoclinic angle $\beta = 90.48^\circ$ is slightly smaller than that in the experiment (91.59°). The differences of crystal parameters between our DFT calculations and the XRD data are below 3% and can be attributed to the approximate nature of the PBE exchange-correlation functional, as has been well documented in the computational chemistry community [30, 31, 32]. It is also found that the discrepancy of the lattice parameter in the b direction is slightly larger than in the other two directions. This can be attributed to the inappropriate description of the van der Waals force between

the interlayer water molecules and the WO_6 octahedra in the b direction arising from the use of the PBE exchange correlation functional in our calculations [18].

To further verify that the generated crystal structure is reasonable, we calculated the reaction enthalpy of the dehydration reaction $WO_3 \cdot 2\,H_2O \longrightarrow WO_3 \cdot H_2O + H_2O(l)$, defined by:

$$\Delta H = H[WO_3 \cdot H_2O] + H^{\circ}[H_2O(l)] - H[WO_3 \cdot 2\,H_2O] \tag{2.3}$$

where $H[WO_3 \cdot H_2O]$, $H[WO_3 \cdot 2\,H_2O]$ and $H[H_2O(l)]$ are the enthalpies of crystalline $WO_3 \cdot H_2O$ and $WO_3 \cdot 2\,H_2O$, and liquid H_2O, respectively. The enthalpies of $WO_3 \cdot H_2O$ and $WO_3 \cdot 2\,H_2O$ can be well approximated by the DFT total energies whereas accurate enthalpy value for liquid H_2O is difficult to obtain from DFT directly. Here, we approximated $H^{\circ}[H_2O(l)]$ by using the reaction enthalpy ΔH_r° (3 kJ/mol) of another dehydration reaction, $WO_3 \cdot H_2O \longrightarrow WO_3 + H_2O(l)$, under standard conditions [33], and the DFT total energies of $WO_3 \cdot H_2O$ and WO_3:

$$H^{\circ}[H_2O(l)] \approx E[WO_3 \cdot H_2O] - E[WO_3] + \Delta H_r^{\circ}. \tag{2.4}$$

The reaction enthalpy obtained from Eq. (2.3) is 36 kJ/mol, while the experimentally measured value is 40 kJ/mol [23]. This good agreement is an indirect justification of the validity of our computational methodology.

With the same space group ($P2_1/n$) as tungsten oxide dihydrate, the room-temperature monoclinic phase of tungsten oxide (γ-WO_3) is characterized by a three-dimensional (3D) network of corner-sharing WO_6 octahedra that are aligned along the b axis, as shown in Figure 2.2a. W ions are off-center in the octahedra, which results in six different W-O bond lengths (see Figure 2.2b). The W-O bond lengths in the a direction are approximately the same (1.89 and 1.94 Å), while in the b and c directions the W-O distances vary from 1.78 to 2.16 Å. These distortions have been attributed to a second order Jahn-Teller effect [34].

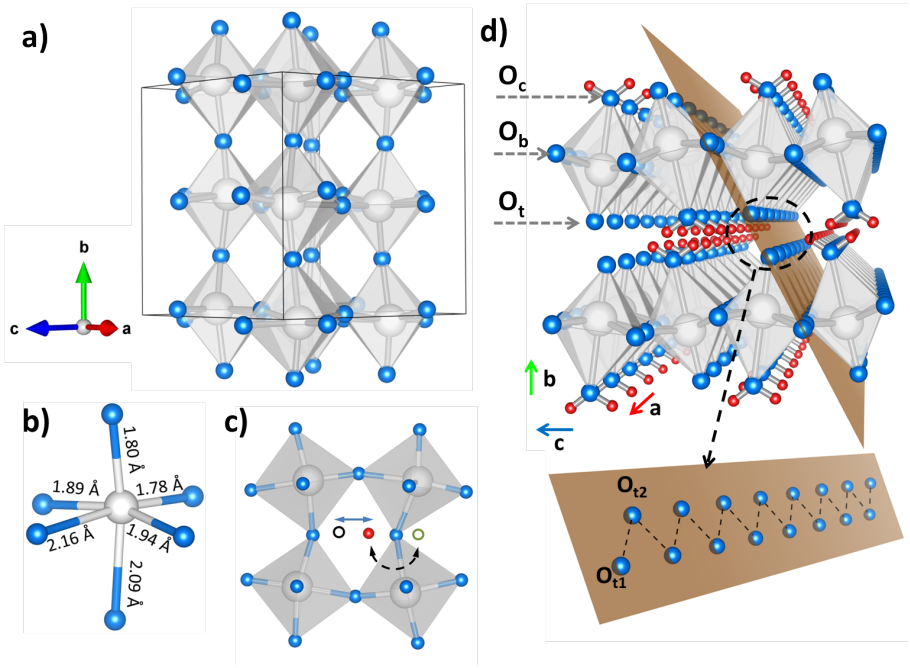

Figure 2.2: (a) Crystal structure of anhydrous monoclinic γ-phase of tungsten oxide, γ-WO_3. (b) An octahedron in γ-WO_3. (c) Proton diffusion in γ-WO_3. (d) Crystal structure of monoclinic tungsten oxide monohydrate, $WO_3 \cdot H_2O$.

Tungsten oxide monohydrate differs from the dihydrate by the absence of the hydrogen-bonded interstitial water layer, but it contains a similar network of corner-sharing WO_6 octahedra with three types of oxygen ions (see Figure 2.2d): bridging oxygen ions (O_b) connecting the octahedra within the layer, each shared by two W^{6+} ions, and terminating and coordinated oxygen ions (O_t and O_c, respectively) on the opposite tips of each WO_6 octahedron; O_c is bonded to two hydrogen ions, forming a water molecule. We point out that the O_t oxygen ions are arranged in one-dimensional (1D) rows running along the *a* direction and, as will be shown below, these rows act as easy diffusion channels in the dilute limit.

2.3.2 Electronic structure

Tungsten oxide dihydrate is predicted to be a direct-gap semiconductor with a calculated PBE band gap of 1.16 eV, as shown in Figure 2.3. For comparison,

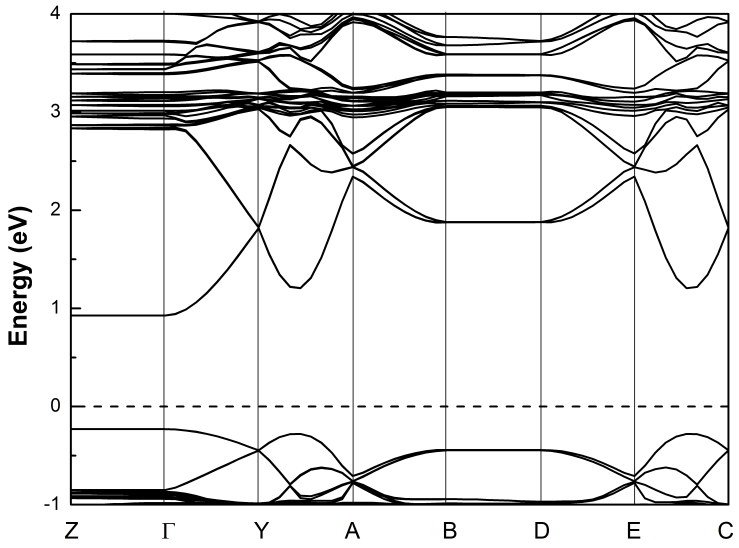

Figure 2.3: Band structure of tungsten oxide dihydrate. The high symmetry points in the b direction are plotted in the range from Z (0, 1/2, 0) to Γ (0, 0, 0) and from B (0, 0, 1/2) to D (0, 1/2, 1/2).

the calculated values of band gaps for $WO_3 \cdot H_2O$ and γ-WO_3 are 0.85 and 1.34 eV (See Figure 2.4 and 2.5), significantly smaller than the experimental values of 2.17 eV and 2.6 eV, respectively [35, 36, 37]. To the best of our knowledge, experimental values of the band gap of $WO_3 \cdot 2\,H_2O$ have not been reported. Since the color of dihydrate samples is yellow [38], the band gap is expected to be larger than 2 eV. It is well understood that nonlocal exchange correlation (xc) functionals are needed to achieve satisfactory agreement between the calculated and experimental band gaps in WO_3 [39, 40]. However, intercalation voltages and diffusion barriers, which are of main interest here, are expected to be less sensitive to nonlocal xc corrections if the additional electrons occupy delocalized d bands [41]. Good agreement between the calculated and experimentally measured intercalation voltages obtained below *a posteriori* justifies our use of the semi-local PBE functional. Finally, we note that the electronic bands of both hydrates are flat in the direction perpendicular to the octahedral layers (see Figure 2.3 and 2.4), indicating that there is practically no wave function overlap across the gap between the layers.

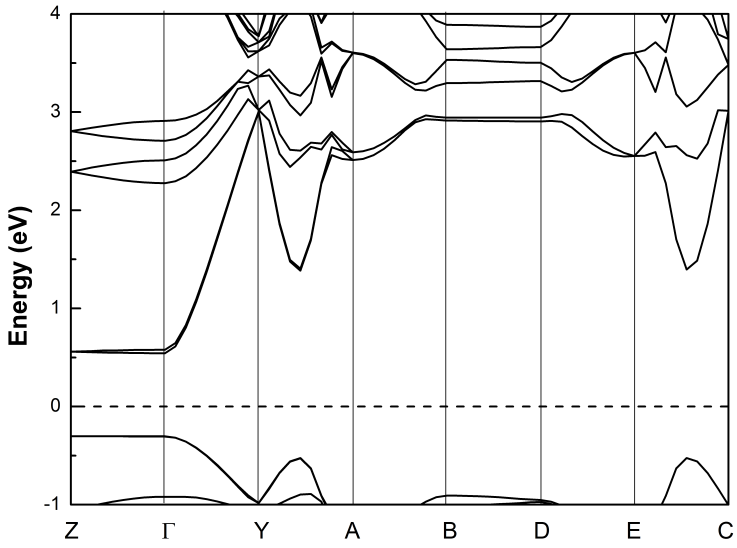

Figure 2.4: Band structure of tungsten oxide monohydrate.

The calculated electronic density of states (eDOS) of $WO_3 \cdot 2\,H_2O$ is shown in Figure 2.6a, and the atom- and angular momentum-decomposed eDOS can be found in Figure 2.7. The energy bands can be divided into three groups: a) states between -20 and -16 eV below the Fermi level, mainly originating from the oxygen $2s$ orbitals, b) states between -8 and 0 eV, chiefly formed by the oxygen $2p$ orbitals, and c) bands above the Fermi level of predominantly tungsten $5d$ character. Specifically, the deep-lying valence bands from -20 to -19 eV are due to the $2s$ orbitals of the O_i/O_c ions. Both the O_t and O_b $2s$ orbitals are overlapped by W $5d$, $6s$, $6p$ orbitals in the octahedral field, yielding σ bonded states in the region from -18 to -16 eV. The sharp peaks in the range from -8 to -7 eV originate from σ bonding hybrids between O_i/O_c $2p$ orbitals and H $1s$ orbitals. States between -7 and -1.5 eV are σ/π bonding hybrids formed by hybridizing O $2p$ and W $5d$ orbitals, and the corresponding antibonding hybrids are in the conduction bands between 1 and 9 eV. We observe that the peaks in the -1.5 to -0.5 eV range are from the nonbonding p orbitals of the O_b ions, which point perpendicular to the tungsten-oxygen octahedral layers. They are shown to play an important role in the proton adsorption and diffusion mechanisms described

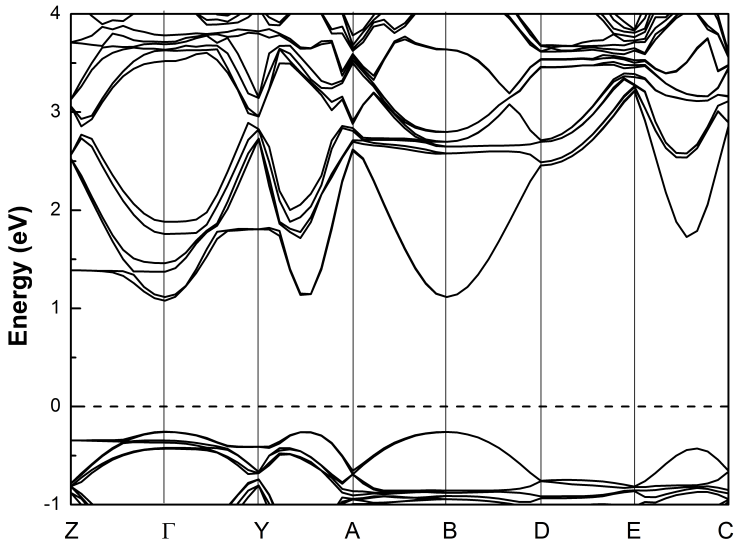

Figure 2.5: Band structure of tungsten oxide.

in Section 2.3.4.

2.3.3 Proton intercalation sites in dihydrate

The candidate intercalation sites for external protons in $WO_3 \cdot 2\,H_2O$ were determined by constructing a regular real-space mesh with a spacing of 0.2 Å and choosing those grid points that satisfy the following criteria: (1) the distance between the extra proton and at least one oxygen ion is between 0.8 and 1.8 Å, (2) the distance between a tungsten ion and the additional proton is above 1.2 Å, and (3) the distance between a native hydrogen ion and the intercalated proton is larger than 1.0 Å. These criteria take into account the fact that hydrogen and tungsten ions are positively charged and therefore repel each other and that stable proton intercalation sites will be near the O^{2-} anions. For all sites satisfying these criteria, the structure was relaxed to the local energy minimum. Figure 2.8 shows the free energies of proton intercalation in $WO_3 \cdot 2\,H_2O$ for different sites at 298 K. The spread of the energies for each type of oxygen site in Figure 2.8 is due to the intrinsic distortion of the WO_6 octahedra and due to the different orientations of the two types of water molecules near the intercalation sites. As discussed in

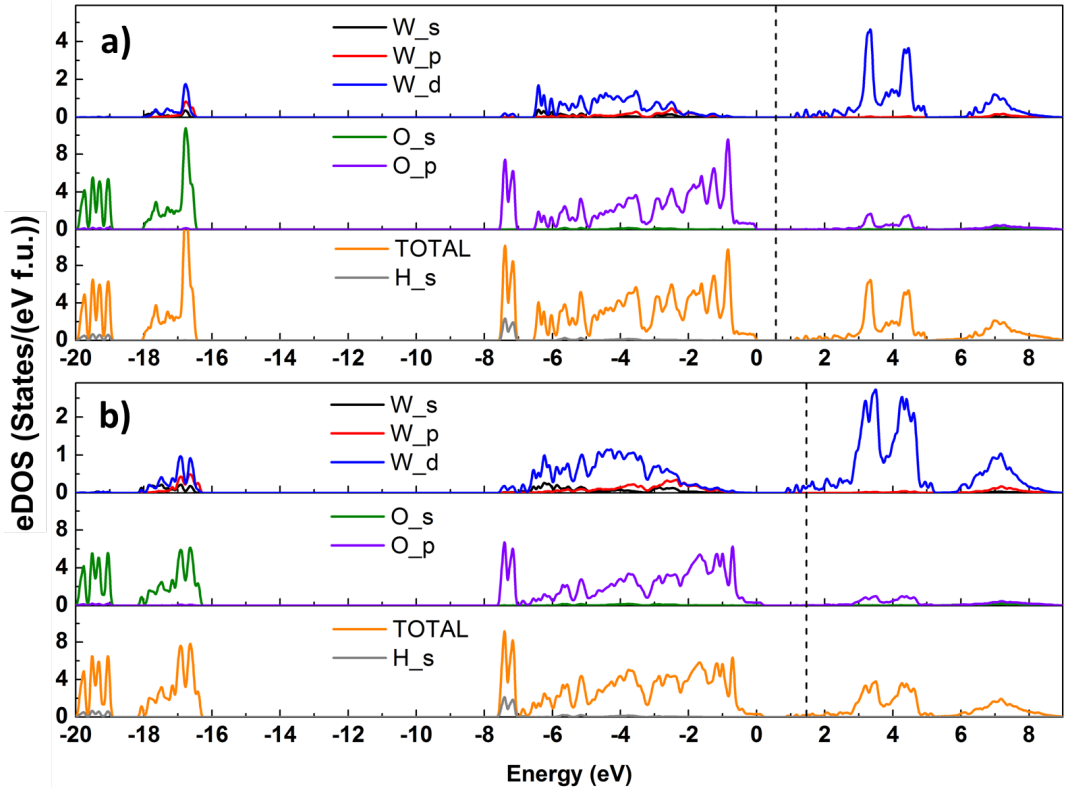

Figure 2.6: Electronic density of states (eDOS) of (a) pure tungsten oxide dihydrate and (b) proton-intercalated tungsten oxide dihydrate. The fermi levels are indicated by dashed lines.

Section 2.3.1 and Figure 2.1, there are four types of oxygen sites in $WO_3 \cdot H_2O$. It was found that protons prefer the bridging oxygen sites, where the lowest free energy is -0.12 eV, corresponding to a proton insertion voltage of 0.12 V. For the other three types of oxygen sites, the free energies are positive, indicating that proton adsorption at these oxygen sites is thermodynamically unfavorable at 298 K. Specifically, a proton at the O_c site is both thermodynamically unfavorable and kinetically unstable, because it repels the coordinated water oxygen while relaxing towards and bonding to either one of the terminating oxygen ions or to an oxygen ion in the interlayer water.

The proton-intercalated structure with the lowest total energy was used for further electronic structure analysis. After introducing a hydrogen atom into the system, tungsten oxide dihydrate becomes metallic (see Figure 2.6b). In compar-

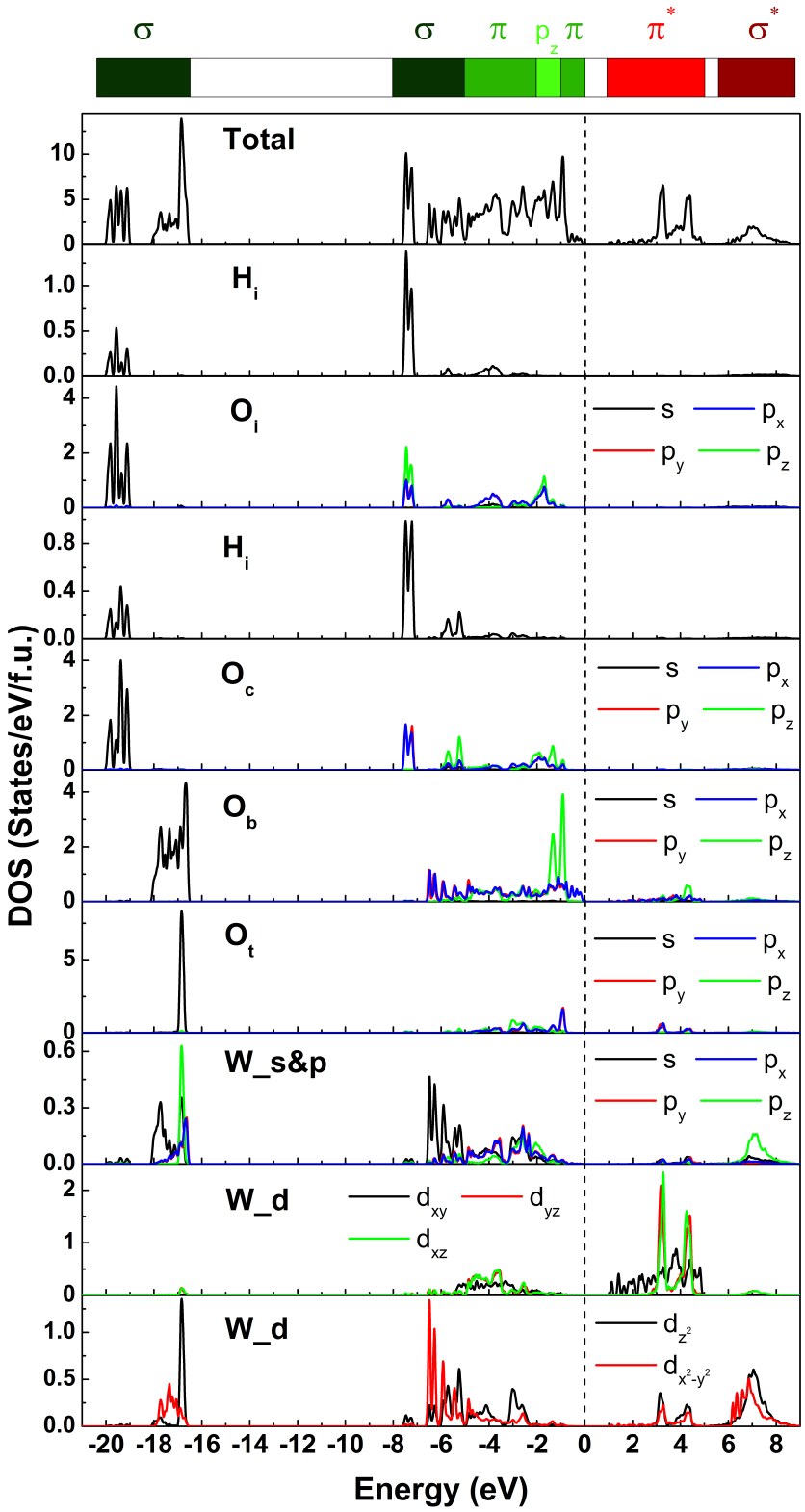

Figure 2.7: The atom- and angular momentum-decomposed electronic density of states.

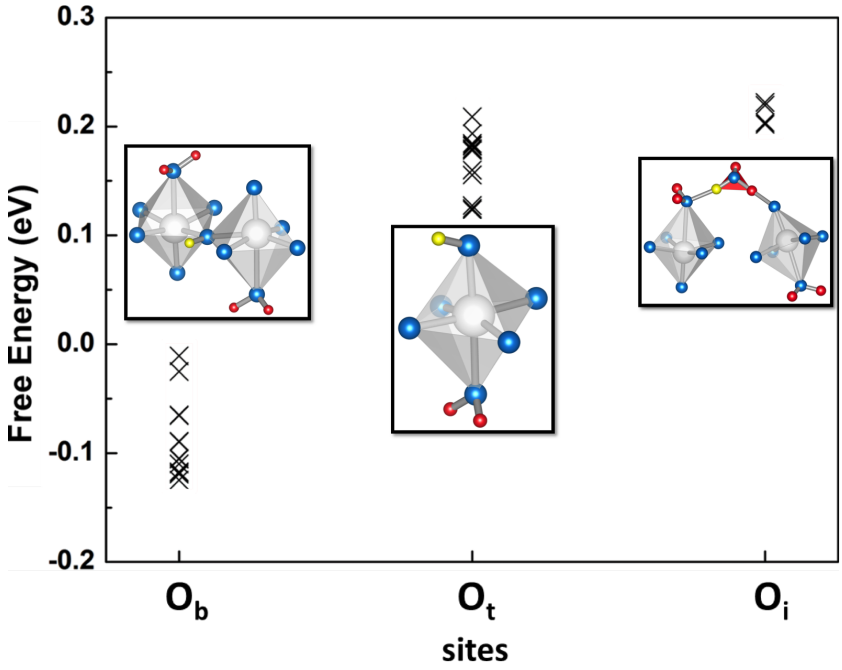

Figure 2.8: Free energies of proton intercalation in $WO_3 \cdot 2\,H_2O$. Inserted protons are shown in yellow.

ison with the electronic density of states (eDOS) of pure $WO_3 \cdot 2\,H_2O$, the eDOS of proton-intercalated $WO_3 \cdot 2\,H_2O$ shifts the Fermi level from the band gap to the bottom of the conduction band formed by empty π^* bonding originating from W $5d$ and bridging oxygen $2p$ orbitals. This interpretation is further supported by visualizing the electronic charge density distribution of the extra electron (shown in Figure 2.9). It can be seen that this electron is largely confined around the O-H group with some delocalization into the W $5d_{xy}$ orbitals within the same tungsten layer. The extra electron charge density does not delocalize between the layers because there is no wave function overlap across the gap, in agreement with the existence of a flat band dispersion perpendicular to the layers (see Figure 2.3). The formation of small polarons is not expected in $WO_3 \cdot 2\,H_2O$ because the structure of the WO_6 octahedra is similar to that in crystalline WO_3, and polarons are not favored in the latter [42, 43].

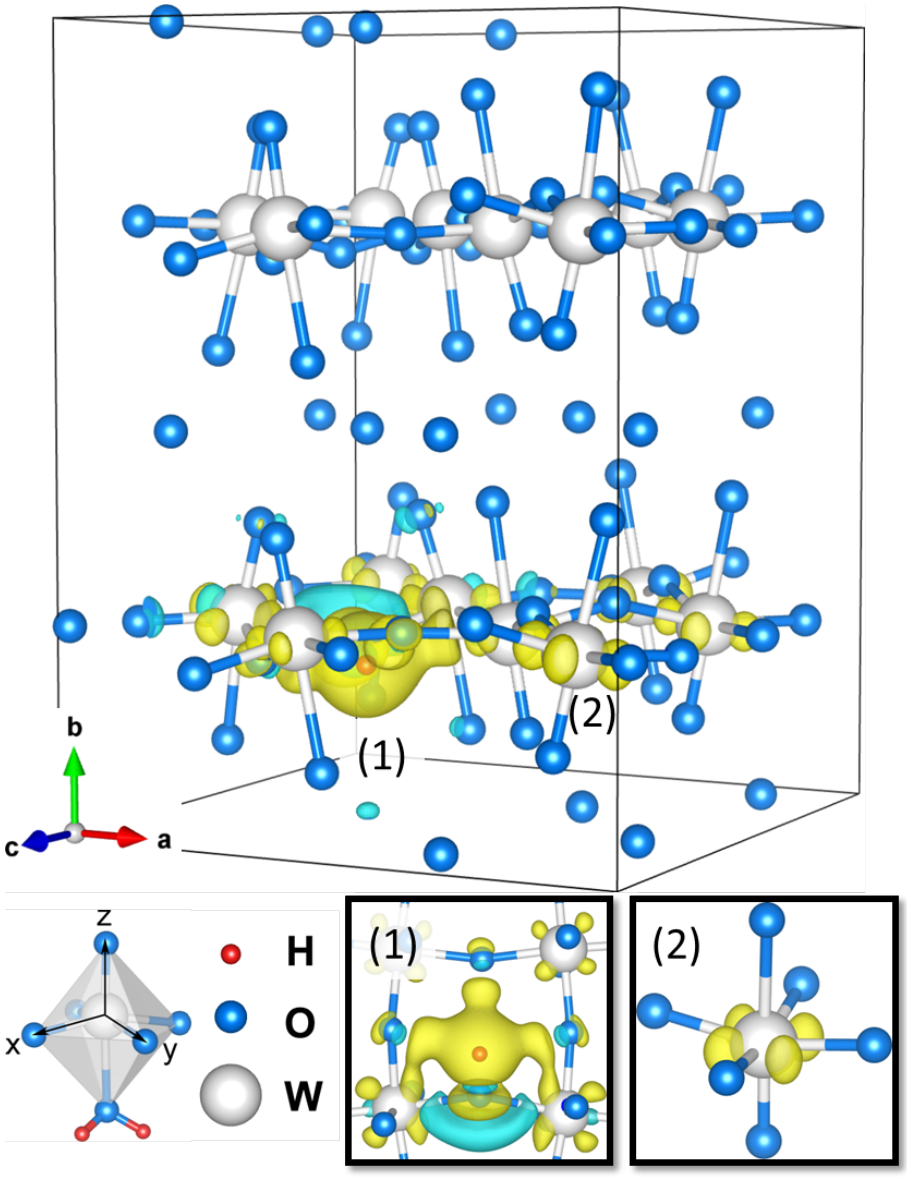

Figure 2.9: Charge density distribution of an additional electron in proton-intercalated $WO_3 \cdot 2\,H_2O$ relative to $WO_3 \cdot 2\,H_2O$. To facilitate the comparison, the ions in $WO_3 \cdot 2\,H_2O$ are fixed to their positions in proton-intercalated $WO_3 \cdot 2\,H_2O$. For visual clarity, the hydrogen ions are not shown except the inserted proton (red). The electron accumulation region is shown in yellow while the depletion region is green. To describe the d orbitals in the WO_6 octahedra, a new coordinate system, rotated by 45 degrees around the b axis, is introduced.

2.3.4 Proton diffusion

2.3.4.1 $WO_3 \cdot 2H_2O$.

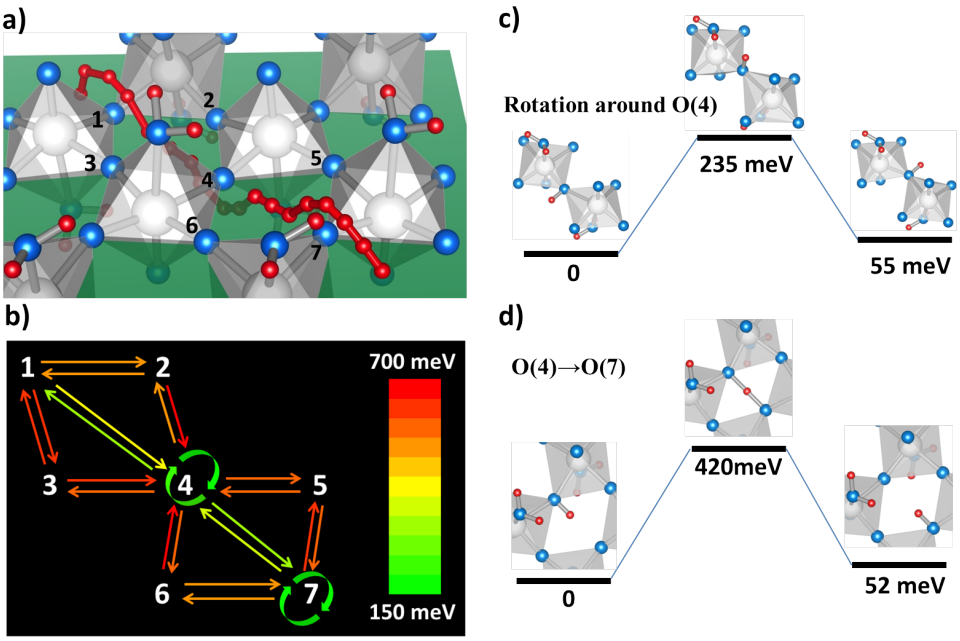

Figure 2.10: Proton diffusion in dihydrate: a) diffusion path, b) activation barriers, and transition states of c) proton rotation around O(4) and d) proton hopping from O(4) to O(7).

In water and in hydrates where water molecules form hydrogen bonds, proton diffusion can proceed via the Grotthuss mechanism [44]. In this mechanism, a proton is transferred from hydronium H_3O^+ to another water molecule via an intermediate formation of a Zundel cation $H_5O_2^+$, which consists of two water molecules sharing a proton. Unexpectedly, we do not observe this mechanism in $WO_3 \cdot 2\,H_2O$. There are two reasons for this behavior. First, a coordinated water molecule is not able to form a Zundel cation ($H_5O_2^+$) with another water molecule, because the O_c ion is one of the ligands in the WO_6 octahedron and reorientation of a coordinated water molecule costs too much energy. Second, the nearest-neighbor distance between two O_i ions is 3.55 Å, while the formation of $H_5O_2^+$ usually requires much closer O-O distances on the order of 2.6∼2.8 Å [45].

Instead of the Grotthuss mechanism, proton diffusion in $WO_3 \cdot 2\,H_2O$ proceeds through the octahedral tungsten oxide layer, shaded green in Figures 2.1a and 2.10a. The proton diffusion path is shown red in Figure 2.10a and the relevant O_b ions within the WO_6 layer are labelled O(1) through O(7). The diffusion mechanism consists of two steps. In the first step, the proton starts out at a site near a bridging O_b ion shared by two WO_6 octahedra, such as near the O(1) ion in the upper-left corner of Figure 2.10a. Then the proton rotates approximately 180 degrees around the W-O_b-W axis [W-O(1)-W in Figure 2.10a]. This rotation is facilitated by the fact that the proton remains bonded to one of the bridging oxygen's nonbonding $2p$ orbitals, which rotates with the proton, as can be seen in the atom- and momentum-decomposed eDOS curves (see Figure 2.11). To accommodate the proton in the final state, there are pronounced rotations of the surrounding octahedra around the b axis, which widen the angle O(3)-O(1)-O(2) and create a local environment for the proton that is similar to the initial state. To examine if the strain caused by these octahedral rotations can be relaxed in a bulk solid, a larger supercell containing 32 formula units was used to verify the results. The calculated activation barrier for proton rotation in the larger supercell is 0.21 eV, which agrees well with the values obtained from the smaller 16 formula unit supercell. It also shows that the corner-linked octahedral layer is quite flexible with respect to correlated rotations of the octahedra.

In the second step, the proton hops towards the diagonal bridging oxygen site, e.g., from O(1) to O(4) or from O(4) to O(7) in Figure 2.10a. The small difference in the energy barriers for the O(1)→O(4) and O(4)→O(7) hops, shown in Figure 2.10b, is caused by the different arrangement of coordinated water molecules in the octahedra and by the intrinsic distortions of the octahedra. After the second step, the proton rotates again as in the first step. The total activation energy for this two-step process is 0.42 eV, which is in good agreement with the value of 0.36 eV deduced from experimental measurements [23].

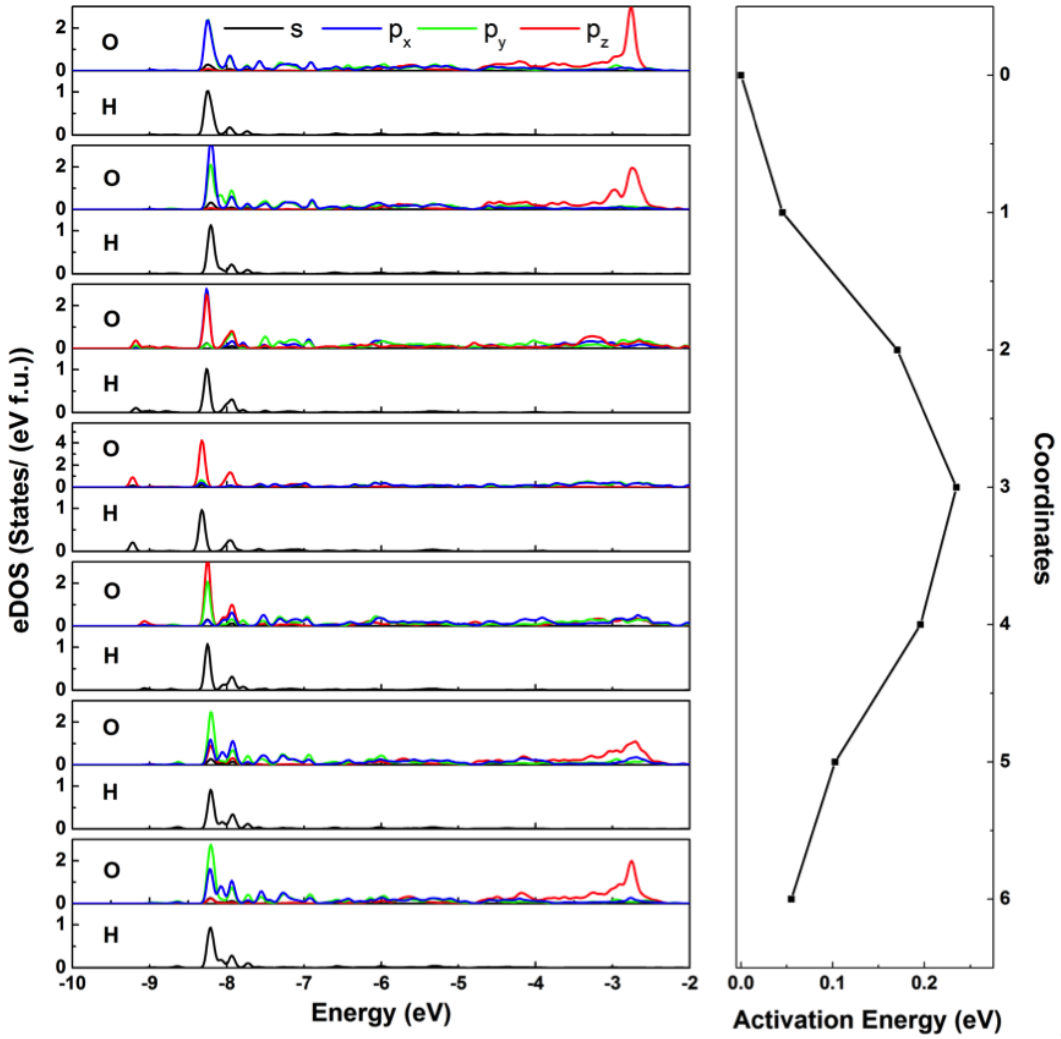

Figure 2.11: Atom- and momentum-decomposed eDOS of the Ob-H dimer during proton rotation. This rotation is facilitated by the fact that the proton remains bonded to one of the bridging oxygen's nonbonding $2p$ orbitals.

Hopping between neighboring oxygen sites in the (010) plane [for instance, from O(4) to O(5) or from O(4) to O(6)] has a significantly higher energy than the two-step process outlined above because the corresponding transition state involves large distortions of the WO_6 octahedra. Hence, protons prefer to move diagonally as plotted in Figure 2.10b. Although the two-step diffusion process represents a one-dimensional diffusion pathway, the diffusion as a whole is two-dimensional due to the symmetry of the WO_6 layer. Indeed, the described mechanism also works for proton diffusion in the perpendicular O(5)→O(6) direction.

2.3.4.2 γ-WO_3.

Since a proton diffuses through the octahedral layer in the dihydrate without direct participation of the structural water molecules, it is reasonable to expect that a similar proton diffusion mechanism should operate in other structurally related tungsten oxides, in particular γ-WO_3. As expected, we find that the proton diffusion in γ-WO_3 also follows the same two-step process as that in the dihydrate (see Figure 2.2c). The barrier for the proton rotation step indicated by the dashed black arrow in Figure 2.2c is 0.12 eV, while the hop (labelled by the solid blue arrow) has an activation energy of 0.35 eV. This process results in an activation energy of 0.35 eV for proton diffusion in γ-WO_3, in good agreement with the value of 0.4 eV measured by Randin *et al* [46]. The predicted proton insertion voltage in γ-WO_3 is 0.11 V, which reproduces the redox peak position (0.2 V relative to SHE) in published cyclic voltammetry measurements with slow sweep rates [20].

2.3.4.3 $WO_3 \cdot H_2O$.

In the dilute limit ($H_yWO_3 \cdot H_2O$, $y = 0.06$), the calculations predict that the proton adsorption energy at the O_t site is 0.25 eV lower than at the O_b site. In

the absence of structural water, the O_t-H dimer points to the nearest O_t, i.e., O_{t1}-H points to O_{t2} in Figure 2.2d. A zigzag chain formed by the O_t ions along the [100] direction acts as a fast proton diffusion channel with an activation energy of only 0.07 eV, much lower than the calculated activation energies in γ-WO_3 and $WO_3 \cdot 2\,H_2O$. Even though this value suggests that transport of individual protons in defect-free monohydrate crystals can be very fast, we will argue below that the presence of crystalline defects and strong repulsive interactions with other protons are likely to slow the diffusion significantly due to the one-dimensional fast diffusion pathways.

We first discuss the energetics of proton adsorption. Using $10.8 \times 10.7 \times 10.4$ Å supercells with 16 formula units, the calculated dilute limit voltages of proton intercalation at the O_t and O_b sites are 1.18 V and 0.93 V, respectively. These numbers are much higher than those in γ-WO_3 and $WO_3 \cdot H_2O$, showing that proton intercalation is energetically highly favorable and suggesting that the dilute limit is not relevant to the conditions used in experimental kinetic measurements. Adding an additional proton to the supercell (corresponding to a concentration $y = 0.13$ in $H_yWO_3 \cdot H_2O$) changes the energetics dramatically: the second proton prefers to adsorb at the bridging oxygen site and the lowest energy configuration corresponds to an intercalation voltage of 0.11 V. This calculation shows that the mutual repulsion of protons is very strong, most likely due to poor screening of the positive charges of the intercalated protons. The calculated diagonal entries of the high-frequency dielectric tensor $\epsilon^{\infty}_{\alpha\beta}$ are 5.3, 3.3, and 5.5, lending support to this idea. The diagonal entries of the static dielectric tensor $\epsilon^{0}_{\alpha\beta}$ are calculated to be 182.0, 4.6, and 50.9. The high values for the in-plane screening are reflective of the easy deformability of the WO_6 octahedral layer, while in the direction perpendicular to the layers the screening remains small. While the values of the dielectric constants are suggestive, the most persuasive evidence for strong proton-proton repulsion comes for the pronounced concentration dependence of

the calculated intercalation voltages.

The atomic configuration of the O_b-H dimer is practically the same as in the dihydrate (see Figure 2.8). The activation energy for proton diffusion within the octahedral layers is found to be 0.52 eV, significantly higher than the value calculated for the zigzag chain, but comparable with the activation energies in γ-WO_3 and $WO_3 \cdot H_2O$. The calculated migration barrier between the O_t and O_b sites is very high (0.95 eV) and hence difficult to overcome at ambient conditions. This indicates that the O_t-O_t and O_b-O_b diffusion paths are isolated and protons cannot make a transition from one to the other.

We hypothesize that with increasing proton concentration all of the one-dimensional zig-zag channels will be eventually blocked by one or more protons adsorbed within the octahedral layers at one of the nearby O_b sites. For the channel to re-open, these bridge-site protons have to diffuse *within* the layer, which requires the two-step process shown in Figure 2.10. A key element in the first (O-H rotation) step of this mechanism is a concerted rotation of the surrounding WO_6 octahedra around the b axis to make space for the proton in the final state. While it is relatively inexpensive in the dilute limit, the presence of additional protons will hinder the rotation because it would not allow compressing the O_b-O_b-O_b angle at their adsorption sites. We have attempted to quantify the energetic cost of such an event, but unfortunately have not been able to obtain a converged transition state structure using the NEB method. Systematic studies of proton diffusion at high concentrations would be interesting, but are beyond the scope of this paper.

To summarize, we propose that the mere presence of fast diffusion pathways in the monohydrate does not guarantee good proton transport properties. Due to the much stronger preference for proton uptake and due to weak screening of Coulomb interactions, repulsive interactions between the intercalated protons are likely to block the fast one-dimensional diffusion channels as well as inhibit the

two-dimensional diffusion observed in γ-WO_3 and $WO_3 \cdot H_2O$. Presence of structural defects, which are thermodynamically favored in sufficiently large samples, is likely to further degrade the diffusion kinetics through the one-dimensional zig-zag channels in a manner similar to the well-studied case of olivine battery materials [47].

2.4 Conclusions

In summary, crystal structures, electronic properties, hydrogen intercalation energetics, and migration barriers in the $WO_3 \cdot xH_2O$ ($x = 0, 1,$ and 2) family of hydrated oxides have been investigated using DFT calculations. In contrast to the naïve expectation that proton diffusion in hydrates should occur via the Grotthuss mechanism, our results show that the intercalated proton diffuses through the layers of corner-sharing WO_6 octahedra and does not involve the hydrogen-bonded H_2O network in $WO_3 \cdot 2\,H_2O$. There are several factors that combine to produce this interesting behavior: (1) intercalated protons prefer to bind to one of the bridging oxygen sites due to the existence of non-bonded $2p$ orbitals, (2) a hydronium ion in the water layer is thermodynamically unstable, and (3) the distortion of the octahedral WO_6 layer introduced by the adsorbed proton can be relaxed in a small region, resulting in lower proton migration barriers. The same diffusion mechanism and similar proton migration barriers have been found in the room-temperature γ-phase of WO_3. In contrast, the monohydrate $WO_3 \cdot H_2O$ follows different mechanisms of proton diffusion. In the dilute limit, the intercalated proton diffuses along one-dimensional zig-zag pathways running in the [100] direction between the octahedral layers. The zig-zag pathways are formed by apical O_t ions and the calculated migration barrier is only 0.07 eV. Due to the stronger energetic preference for proton absorption, a much higher concentration of protons is predicted to exist in $H_yWO_3 \cdot H_2O$ under typical experimental conditions. At

non-dilute concentrations, our results indicate that strong repulsive interactions exist between the intercalated protons. We hypothesize that proton-proton repulsion in combination with structural defects will block the fast one-dimensional diffusion channels, while the presence of a high concentration of protons in the octahedral layers will hinder the rotation step necessary for the two-dimensional intralayer mechanism operating in $WO_3 \cdot 2\,H_2O$. This argument provides insight into the reasons why bulk proton transport in $WO_3 \cdot H_2O$ is suppressed, as indicated by experimental measurements which can only detect a surface contribution [23].

References

[1] Patrice Simon and Yury Gogotsi. Materials for electrochemical capacitors. *Nature materials*, 7(11):845–854, 2008.

[2] John R Miller and Andrew F Burke. Electrochemical capacitors: challenges and opportunities for real-world applications. *The Electrochemical Society Interface*, 17(1):53, 2008.

[3] Iris E. Rauda, Veronica Augustyn, Bruce Dunn, and Sarah H. Tolbert. Enhancing pseudocapacitive charge storage in polymer templated mesoporous materials. *Accounts of Chemical Research*, 46(5):1113–1124, 2013.

[4] B.E. Conway. *Electrochemical Supercapacitors : scientific fundamentals and technological applications*. Springer, april 1999.

[5] Sergio Trasatti and Giovanni Buzzanca. Ruthenium dioxide: A new interesting electrode material. solid state structure and electrochemical behaviour. *Journal of Electroanalytical Chemistry and Interfacial Electrochemistry*, 29(2):A1 – A5, 1971.

[6] JP Zheng, PJ Cygan, and TR Jow. Hydrous ruthenium oxide as an electrode material for electrochemical capacitors. *Journal of The Electrochemical Society*, 142(8):2699–2703, 1995.

[7] Wataru Sugimoto, Katsunori Yokoshima, Yasushi Murakami, and Yoshio Takasu. Charge storage mechanism of nanostructured anhydrous and hydrous ruthenium-based oxides. *Electrochim. Acta*, 52(4):1742–1748, 2006.

[8] Vidvuds Ozoliņš, Fei Zhou, and Mark Asta. Ruthenia-based electrochemical supercapacitors: Insights from first-principles calculations. *Acc. Chem. Res.*, 46(5):1084–1093, 2013.

[9] C.J.T. de Grotthuss. Memoir upon the decomposition of water, and of the bodies which it holds in solution, by means of galvanic electricity. *Philos. Mag. (London)*, 25:330–339, 1806.

[10] Takeshi Ueki and Masayoshi Watanabe. Macromolecules in ionic liquids: Progress, challenges, and opportunities. *Macromolecules*, 41(11):3739–3749, 2008.

[11] Philippe Colomban. *Proton Conductors: Solids, Membranes and Gels - Materials and Devices*. Cambridge University Press, September 1992.

[12] W. Munch, G. Seifert, K.D. Kreuer, and J. Maier. A quantum molecular dynamics study of proton conduction phenomena in $BaCeO_3$. *Solid State*

Ionics, 8688, Part 1(0):647 – 652, 1996. Proceedings of the 10th International Conference on Solid State Ionics.

[13] K.D Kreuer. Aspects of the formation and mobility of protonic charge carriers and the stability of perovskite-type oxides. *Solid State Ionics*, 125(14):285 – 302, 1999.

[14] Richard M Martin. *Electronic structure: basic theory and practical methods*. Cambridge university press, 2004.

[15] Pierre Hohenberg and Walter Kohn. Inhomogeneous electron gas. *Physical review*, 136(3B):B864, 1964.

[16] Walter Kohn and Lu Jeu Sham. Self-consistent equations including exchange and correlation effects. *Physical Review*, 140(4A):A1133, 1965.

[17] J. P. Perdew and Alex Zunger. Self-interaction correction to density-functional approximations for many-electron systems. *Phys. Rev. B*, 23:5048–5079, May 1981.

[18] John P Perdew, Kieron Burke, and Matthias Ernzerhof. Generalized gradient approximation made simple. *Phys. Rev. Lett.*, 77(18):3865–3868, 1996.

[19] John P Perdew and Yue Wang. Accurate and simple analytic representation of the electron-gas correlation energy. *Physical Review B*, 45(23):13244, 1992.

[20] A Di Paola, F Di Quarto, and C Sunseri. Electrochromism in anodically formed tungsten oxide films. *J. Electrochem. Soc.*, 125(8):1344–1347, 1978.

[21] Zhong Xie, Lina Gao, Bo Liang, Xianfu Wang, Gui Chen, Zhe Liu, Junfeng Chao, Di Chen, and Guozhen Shen. Fast fabrication of a $WO_3 \cdot 2\,H_2O$ thin film with improved electrochromic properties. *J. Mater. Chem.*, 22(37):19904–19910, 2012.

[22] Wataru Sugimoto, Takeo Kizaki, Katsunori Yokoshima, Yasushi Murakami, and Yoshio Takasu. Evaluation of the pseudocapacitance in RuO_2 with a RuO_2/gc thin film electrode. *Electrochim. Acta*, 49(2):313–320, 2004.

[23] YM Li, M Hibino, M Miyayania, and T Kudo. Proton conductivity of tungsten trioxide hydrates at intermediate temperature. *Solid State Ionics*, 134(3):271–279, 2000.

[24] Peter E Blöchl. Projector augmented-wave method. *Phys. Rev. B: Condens. Matter*, 50(24):17953–17979, 1994.

[25] Georg Kresse and Jürgen Furthmüller. Efficiency of ab-initio total energy calculations for metals and semiconductors using a plane-wave basis set. *Comp. Mater. Sci.*, 6(1):15–50, 1996.

[26] Hendrik J Monkhorst and James D Pack. Special points for brillouin-zone integrations. *Phys. Rev. B: Condens. Matter*, 13(12):5188–5192, 1976.

[27] H. Jónsson, G. Mills, and K. W. Jacobsen. *Classical and Quantum Dynamics in Condensed Phase Simulations*. World Scientific, June 1998.

[28] Graeme Henkelman, Blas P Uberuaga, and Hannes Jónsson. A climbing image nudged elastic band method for finding saddle points and minimum energy paths. *J. Chem. Phys.*, 113:9901–9904, 2000.

[29] Justin T Fermann and Scott Auerbach. Modeling proton mobility in acidic zeolite clusters: Ii. room temperature tunneling effects from semiclassical rate theory. *J. Chem. Phys.*, 112:6787–6794, 2000.

[30] Martin Fuchs, Michel Bockstedte, Eckhard Pehlke, and Matthias Scheffler. Pseudopotential study of binding properties of solids within generalized gradient approximations: The role of core-valence exchange correlation. *Phys. Rev. B: Condens. Matter*, 57(4):2134–2145, 1998.

[31] M Fuchs, JLF Da Silva, C Stampfl, J Neugebauer, and M Scheffler. Cohesive properties of group-iii nitrides: A comparative study of all-electron and pseudopotential calculations using the generalized gradient approximation. *Phys. Rev. B: Condens. Matter*, 65(24):245212, 2002.

[32] Christopher C Fischer, Kevin J Tibbetts, Dane Morgan, and Gerbrand Ceder. Predicting crystal structure by merging data mining with quantum mechanics. *Nat. Mater.*, 5(8):641–646, 2006.

[33] Malcolm W Chase. *NIST-JANAF thermochemical tables*. American Institute of Physics, 1998.

[34] John B. Goodenough. Metallic oxides. *Prog. Solid State Chem.*, 5(0):145 – 399, 1971.

[35] Peng Wang, Baibiao Huang, Xiaoyan Qin, Xiaoyang Zhang, Ying Dai, and Myung-Hwan Whangbo. $Ag/AgBr/WO_3 \cdot H_2O$: visible-light photocatalyst for bacteria destruction. *Inorg. Chem.*, 48(22):10697–10702, 2009.

[36] F.P. Koffyberg, K Dwight, and A Wold. Interband transitions of semiconducting oxides determined from photoelectrolysis spectra. *Solid State Commun.*, 30(7):433–437, 1979.

[37] E Salje. A new type of electro-optic effect in semiconducting WO_3. *J. Appl. Crystallogr.*, 7(6):615–617, 1974.

[38] Meyer L Freedman. The tungstic acids. *J. Am. Chem. Soc.*, 81(15):3834–3839, 1959.

[39] Yuan Ping, Dario Rocca, and Giulia Galli. Optical properties of tungsten trioxide from first-principles calculations. *Phys. Rev. B: Condens. Matter*, 87(16):165203, 2013.

[40] Fenggong Wang, Cristiana Di Valentin, and Gianfranco Pacchioni. electronic and structural properties of WO_3: a systematic hybrid dft study. *J. Phys. Chem. C*, 115(16):8345–8353, 2011.

[41] F Zhou, M Cococcioni, C Marianetti, D Morgan, and G Ceder. First-principles prediction of redox potentials in transition-metal compounds with LDA+U. *Phys. Rev. B: Condens. Matter*, 70(23):235121, December 2004.

[42] Haidong Zheng, Jian Zhen Ou, Michael S Strano, Richard B Kaner, Arnan Mitchell, and Kourosh Kalantar-zadeh. Nanostructured tungsten oxide–properties, synthesis, and applications. *Adv. Funct. Mater.*, 21(12):2175–2196, 2011.

[43] M Deepa, AK Srivastava, M Kar, and SA Agnihotry. A case study of optical properties and structure of sol–gel derived nanocrystalline electrochromic wo3 films. *J. Phys. D: Appl. Phys.*, 39(9):1885–1893, 2006.

[44] Dominik Marx. Proton transfer 200 years after von grotthuss: Insights from ab initio simulations. *Chem. Phys. Chem.*, 7(9):1848–1870, 2006.

[45] Francis F Muguet. Mcscf vibrational spectra of the symmetric and asymmetric dihydronium cations. *J. Mol. Struc.: Theochem.*, 368:173–196, 1996.

[46] Jean-Paul Randin and René Viennet. Proton diffusion in tungsten trioxide thin films. *J. Electrochem. Soc.*, 129(10):2349–2354, 1982.

[47] Gopi Krishna Phani Dathar, Daniel Sheppard, Keith J. Stevenson, and Graeme Henkelman. Calculations of li-ion diffusion in olivine phosphates. *Chem. Mater.*, 23(17):4032–4037, 2011.